



Cite this: *New J. Chem.*, 2018, 42, 18128

Co²⁺ substituted La₂CuO₄/LaCoO₃ perovskite nanocomposites: synthesis, properties and heterogeneous catalytic performance

M. Sukumar,^a L. John Kennedy,^{ib}*^a J. Judith Vijaya,^{ib}^b B. Al-Najar^c and M. Bououdina^c

Cobalt substituted La₂CuO₄/LaCoO₃ perovskite nanocomposites were prepared using a microwave combustion method. X-ray diffraction analysis showed that Co²⁺ substitution in La₂CuO₄ induced the formation of a secondary LaCoO₃ phase with rhombohedral structure along with the existing orthorhombic (La₂CuO₄) structure. The orthorhombic/rhombohedral structured nanocomposites possessed an average crystallite size in the range of 36–46 nm and 21–49 nm, respectively. The Rietveld analysis confirmed the formation of these two phases. The appearance of FT-IR bands around 682 and 512 cm⁻¹ was correlated to the orthorhombic stretching modes while the bands around 580 and 445 cm⁻¹ were associated with the rhombohedral stretching modes thereby confirming the two-phase perovskite system. An optical study revealed two linear regions depicting two band gaps related to the La₂CuO₄ and LaCoO₃ phases. The band gap was found to increase with an increase in the Co²⁺ doping fraction. Morphological observations using scanning electron microscopy showed intragranular pores and fused grains with distinct grain boundaries. The change in the magnetic properties was associated most probably with the exchange of the A and B sites within the La₂CuO₄ host lattice because of Co²⁺ doping, as well as the important phase composition of La₂CuO₄/LaCoO₃ obtained from the ferromagnetic-to-paramagnetic transition. The BET surface area of the pure and doped nanocomposites was found to vary considerably within the range of 12.2–43.7 m² g⁻¹. The as-fabricated La₂CuO₄/LaCoO₃ perovskite nanocomposites were evaluated for the conversion of glycerol to formic acid in a liquid phase batch reactor under atmospheric conditions. This La³⁺ based nanocomposite behaves as an efficient bifunctional catalyst with high conversion efficiency and selectivity around 96.5% and 95.1%, respectively.

Received 14th August 2018,
Accepted 8th October 2018

DOI: 10.1039/c8nj04133d

rsc.li/njc

1. Introduction

Magnetic nanocomposites, either spinels or perovskites doped with transition and rare earth metal ions, have been investigated for various applications due to their unique structural, electrical and magnetic properties.^{1–5} A₂BO₄ compounds generally have an orthorhombic K₂NiF₄ type structure, with the *Cmca* space group and 4 formula units per unit cell (*Z* = 4).⁶ K₂NiF₄-type (A₂BO₄ = AO + ABO₃) oxides belong to the perovskite family, where A is a large metal cation such as rare earth and alkaline earth metal ions, while B is a transition metal ion

with smaller size. A trivalent rare earth cation occupies the A-site of A₂BO₄, while a divalent cation occupies the B-site, due to electroneutrality of the oxides (A₂³⁺B²⁺O₄²⁻).⁷ In this class, La₂CuO₄ is a perovskite type mixed oxide, having alternating layers of a (LaO)₂ perovskite structure and rock-salt CuO₂ units (La₂³⁺Cu²⁺O₄²⁻).⁸ The A-site (La³⁺) cation has nine-fold coordination and the B-site (Cu²⁺) cation has octahedral coordination, respectively.⁹ La₂CuO₄ is a p-type anti-ferromagnetic semiconductor⁸ that can naturally undergo a structural phase transition from orthorhombic to tetragonal either by doping impurities, by applying pressure or by changing temperature. There are three major structural phases observed in the La₂CuO₄ metal oxide: (i) low temperature tetragonal (LTT), (ii) low temperature orthorhombic (LTO), and (iii) high temperature tetragonal (HTT) with *I*₄/*mmm*, *Bmab*, and *P*₄/*ncm* symmetry, respectively.¹⁰

Another type of perovskite oxide with the formula of ABO₃, where the larger cation at the A-site has 12 coordination and the smaller cation at the B-site has 6 coordination, respectively.^{11,12} This type of perovskite has a typical band gap ranging from 3 to 4 eV.¹³

^a Materials and Physics Division, School of Advanced Sciences, Vellore Institute of Technology (VIT), Chennai Campus, Chennai 600 127, Tamil Nadu, India.
E-mail: jklsac14@yahoo.co.in, ljkenedy14@gmail.com; Fax: 044-39932555;
Tel: +91-44-39931326

^b Catalysis and Nanomaterials Research Laboratory, Department of Chemistry, Loyola College (Autonomous), Chennai 600 034, Tamil Nadu, India

^c Department of Physics, College of Science, University of Bahrain, P.O. Box 32038, Bahrain

LaCoO₃ belonging to the ABO₃ perovskite family is a mixed electronic and oxygen-ion conductor with remarkable electronic structure, thermal stability, ionic conductivity, electron mobility and redox behavior.¹⁴ This type of perovskite structure is perfectly cubic, but the difference in the ionic radius of La³⁺ (1.36 Å) and Co²⁺ (0.9 Å) distorts the cubic structure leading to the appearance of rhombohedral symmetry.¹⁵ LaCoO₃ also exhibits unique electronic phase changing properties with respect to temperature. At room temperature (293 K), LaCoO₃ crystallizes in a rhombohedral structure with the $R\bar{3}c$ space group and a unit cell consisting of 10 atoms.¹⁶ LaCoO₃ undergoes a gradual transition from a diamagnetic to a paramagnetic semiconductor at room temperature while a semiconductor-to-metal transition is also possible at 500–600 K.¹⁷

In recent years, composite materials have gained particular interest because they offer numerous advantages, as they significantly possess enhanced characteristics compared to their individual constituents or conventional materials. In this context, a nanocomposite can be defined as a combination of two or more constituent materials or phases, showing high thermal stability, high strength, chemical resistance, improved catalytic properties and so on.^{18–21} Despite many available nanocomposites, the combination of perovskite based nanocomposites is scarce in the literature. La₂CuO₄ and LaCoO₃ based-perovskite nanocomposites can be synthesized by different physical and chemical routes such as, solid state reaction,^{6,13,22,23} sol-gel,^{8,24} combustion,^{25,26} hydrothermal^{27,28} and high energy ball milling.¹³ These types of perovskite oxides are widely used for catalytic activities^{9,12,25,29,30} and in gas sensors²² and superconductor devices.³¹ The catalytic applications of lanthanum (La³⁺) based materials have higher carbonaceous oxidation activity while cobalt (Co²⁺) containing perovskites exhibit excellent electrochemical properties.²⁸ The role of perovskites as oxidation catalysts may be associated with the high mobility of O²⁻ ions within the crystal lattice and their migration to the surface, and the catalyst can provide additional active sites for the oxidation of carbonaceous substances.³²

Velasquez *et al.* and Villoria *et al.* have prepared La₂CuO₄ and LaCoO₃ perovskites individually by employing a self-combustion method using glycine as a fuel followed by calcination at 700 °C for 6 h and 750 °C for 4 h, respectively.^{25,26} These perovskites have been used for the catalytic oxidation of glycerol and oxidative reforming of diesel. However, reports on the preparation of La₂CuO₄ and LaCoO₃ using a microwave combustion method are scarce. The present study focuses on the synthesis of Co²⁺ doped La₂CuO₄/LaCoO₃ perovskite oxides employing the microwave combustion technique. The effect of Co²⁺ doping on La₂CuO₄ under microwave influence for the appearance of a secondary perovskite phase (LaCoO₃) is examined. In comparison to the conventional heating methods, the microwave combustion method is considered as a rapid process for the synthesis of metal oxide materials.^{33–37} The choice of oxidizer (precursor) and fuel (urea) in a suitable stoichiometric ratio will allow better control over the combustion process. This results in the formation of nanostructures with the desired phase formation and composition, or sometimes with the formation of an unexpected additional phase.³⁸ In such case, the additional phase will disappear when subjected to calcination at moderate temperature.

The role of microwaves in the formation of two perovskite-like systems at a relatively lower temperature and a shorter time was investigated. The synthesized La₂CuO₄/LaCoO₃ perovskite nanocomposites were characterized by several techniques including XRD, FTIR, DRS, HR-SEM, EDX, VSM, TG/DTA and BET techniques in order to determine the structural, optical, and magnetic properties. The nanocomposites were then evaluated for glycerol oxidation to explore their potential future catalytic applications.

2. Experimental

2.1. Synthesis of Co²⁺ doped La₂CuO₄/LaCoO₃ perovskite nanocomposites

La(NO₃)₃·6H₂O, Co(NO₃)₂·4H₂O and Cu(NO₃)₂·3H₂O were used as precursors and NH₂CONH₂ as a fuel for the synthesis of the composites. The precursors for La_{2-x}Co_xCuO₄ and urea constituents in the desired proportions were dissolved in de-ionized water and stirred for 45 min at room temperature to obtain a homogeneous solution. The fuel to oxidizer ratio (F/O) was equal to 1 as per the propellant chemistry concept. The required amount of oxidizer-to-fuel molar ratio for the composition was calculated based on the total oxidizing and reducing valences in the oxidizer (lanthanum nitrate, cobalt nitrate, copper nitrate) and dividing by the sum of the total oxidizing and reducing valences in the fuel (urea) as expressed in the following equation.³⁹

$$\text{Oxidizer/Fuel} = \frac{\sum \text{all oxidizing and reducing elements in oxidizer}}{(-1) \sum \text{oxidizing and reducing elements in fuel}} \quad (1)$$

The homogeneous solution was exposed to microwave energy in a microwave oven at 2.45 GHz, 900 W power for 15 min. Once the temperature reached a threshold level, the precursor solution underwent dehydration and combustion, resulting in a black fluffy powder (LCM). This black powder contained metal hydroxides and other impurity phases (see Fig. 3), and it was subsequently subjected to calcination at 500 °C for 2 h, resulting in the formation of the crystalline La₂CuO₄ and LaCoO₃ phases of the perovskite system. Since the final obtained products consisted of a combination of two perovskite phases, the samples were identified as La₂CuO₄/LaCoO₃ nanocomposites. Fig. 1 shows the schematic representation for the preparation of La₂CuO₄/LaCoO₃ perovskite nanocomposites. The compositions were prepared with the addition of cobalt (Co²⁺) of different molar ratios in a La_{2-x}Co_xCuO₄ system with $x = 0, 0.1, 0.2, 0.3, 0.4$ and 0.5 and the samples are labeled LCC0, LCC1, LCC2, LCC3, LCC4 and LCC5, respectively.

2.2. Characterization

Thermal behaviour of the as-prepared powders was studied by thermogravimetric analysis using an Exstar TG/DTA 7200 instrument from SII Nanotech at a heating rate of 5 °C min⁻¹ under a nitrogen atmosphere. The phase composition has been analysed by X-ray diffraction using a high resolution Rigaku Ultima IV diffractometer with CuK α radiation ($\lambda = 1.5406$ Å). The refinements of the XRD patterns were performed using the

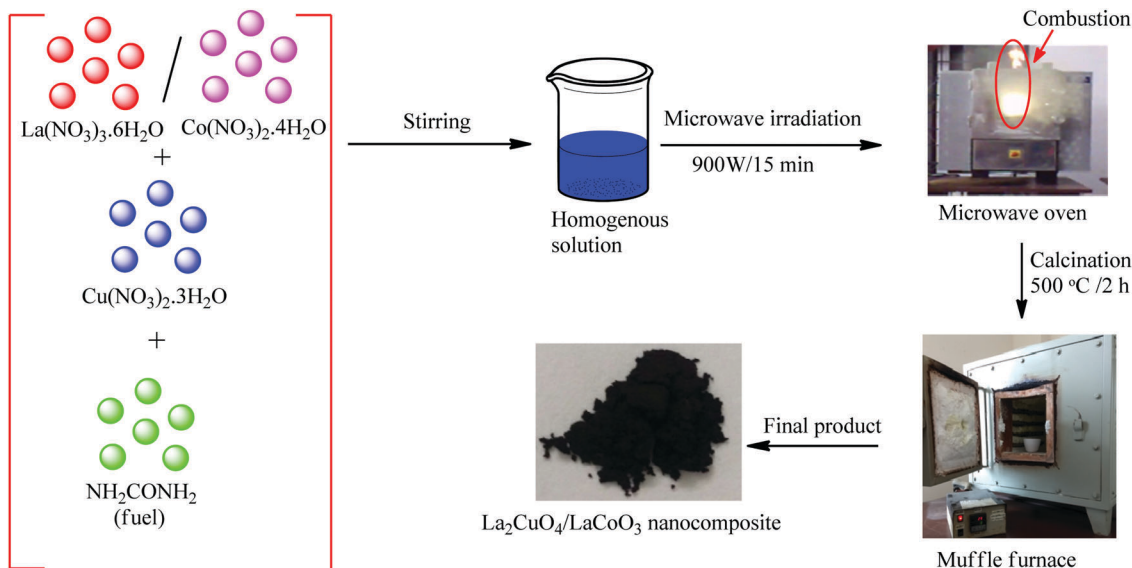


Fig. 1 Schematic representation of the preparation of $\text{La}_2\text{CuO}_4/\text{LaCoO}_3$ perovskite nanocomposites.

PDXL program based on the Rietveld method. A Thermo scientific Nicolet 10 OMNI FTIR spectrophotometer was used for the determination of surface functional groups. Diffuse reflectance UV-visible spectra were recorded using a Thermo scientific Evolution 300 UV-visible spectrophotometer to estimate the energy bandgap. Morphological observations were performed using a HITACHI S4800 high resolution field scanning electron microscope (HR-SEM) equipped with a HORIBA EMAX energy dispersive X-ray (EDX) detector for elemental composition analysis. Magnetic measurements were carried out at room temperature using a PMC MicroMag 3900 model vibrating sample magnetometer (VSM) equipped with a 1 T magnet and the magnetization curves were measured from $-10\,000$ Oe to $10\,000$ Oe. N_2 adsorption-desorption isotherms of the porous double-perovskite nanocomposites were measured using an automatic adsorption instrument (Micromeritics – ASAP 2020 unit). Prior to the measurement, the samples were degassed at 150 °C for 12 h. The nitrogen adsorption-desorption isotherms were recorded at a liquid nitrogen temperature of 77 K .

2.3. Catalytic activity tests

Selective liquid phase oxidation of glycerol was carried out in a batch reactor at atmospheric pressure. The reaction parameters are as follows: 50 mg of $\text{La}_2\text{CuO}_4/\text{LaCoO}_3$ as the catalyst, 50 mmol of glycerol ($\text{C}_3\text{H}_8\text{O}_3$) as the reactant, 50 mmol of hydrogen peroxide (H_2O_2) as the oxidant and dimethyl sulfoxide (DMSO) as the solvent. The above constituents were placed in a round bottom two-necked flask (250 ml) equipped with a water condenser and the temperature was maintained at 70 °C for 6 h and then cooled to room temperature. The obtained product was collected and analyzed using MAYURA 1100 gas chromatography (GC) equipped with an Abel Bonded (AB-1, Capillary) column ($30\text{ m} \times 0.25\text{ mm} \times 0.25\text{ }\mu\text{m}$) with an FID detector. The products were also analyzed by GC-MS using an Agilent Technologies Model 7890A gas chromatograph, coupled to a mass detector model 5975C, with an HP-5MS,

$30\text{ m} \times 250\text{ }\mu\text{m} \times 0.25\text{ }\mu\text{m}$ column. Helium gas was used as the carrier gas at a flow rate of 1.4 mL min^{-1} , with a split ratio of 130/1 and an injector temperature of 25 °C , and the oven temperature profile was 80 °C for 5.0 min and increased to 100 °C with a ramping rate of 3 °C min^{-1} , then maintained at the final temperature for 1 min.

3. Results and discussion

3.1. TG/DTA analysis of the LCM sample

Thermogravimetric analysis of the black fluffy powder (LCM) obtained as such from the microwave oven has been performed to study the thermal behavior. The TG/DTA curve of the LCM sample is given in Fig. 2. A slight weight loss (3%) between 40 and 105 °C can be attributed to dehydration of water molecules on the surface of the particles as confirmed by the appearance of an endothermic peak in the DTA thermogram. The major weight loss (23.2%) occurring between 105 and 460 °C is due to the elimination of the hydroxyl group and other volatile components present in the sample. However, beyond 460 °C , there is only a gradual weight loss occurring in the sample (6.8%), which may be caused by the elimination of tightly bound volatiles or structural rearrangement taking place. Hence, calcination has been performed in the temperature range of 500 to 700 °C .⁴⁰ The results reveal that a single phase (orthorhombic) crystal structure is formed with the studied temperature range. Moreover, the sample calcined at 700 °C does not have much difference in the thermal behavior compared to that of the sample calcined at 500 °C , and hence in the present study, the calcination temperature has been fixed at 500 °C .

3.2. X-ray diffraction analysis

Fig. 3 shows the XRD patterns of the as-prepared $\text{La}_2\text{CuO}_4/\text{LaCoO}_3$ perovskite nanocomposites. The undoped La_2CuO_4 (LCCO) reveals

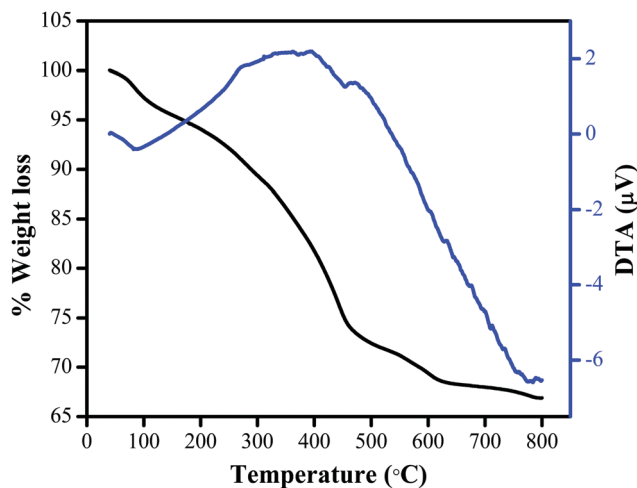


Fig. 2 TG-DTA spectrum of the LCM sample.

a single perovskite phase with an orthorhombic structure (space group *Bmab*, JCPDS No: 88-0940). This indicates that the adopted microwave combustion, followed by calcination at 500 °C for 2 h is sufficient to prepare a single La_2CuO_4 perovskite phase. The characteristic peaks observed at 2θ values around 24.3°, 27.1°, 31.1°, 33.1°, 33.4°, 41.2°, 41.7°, 43.5°, 47.8°, 54.0°, 54.4°, 55.8°, 58.0°, 64.9°, 65.1°, 69.6°, 70.0°, 75.3°, 76.5°, 78.5° are indexed as the (111), (004), (113), (020), (200), (006), (115), (204), (220), (206), (117), (224), (133), (226), (135), (040), (400), (331), (228) and (333) crystallographic planes, respectively. However a different trend was observed upon doping with Co^{2+} . It was found that upon Co^{2+} doping, a new secondary LaCoO_3 perovskite phase appears. The substitution of La^{3+} by Co^{2+} ions results in the formation of two phase-systems with orthorhombic (La_2CuO_4) and rhombohedral (LaCoO_3) structures respectively, indicating the formation of a composite. Other than the appearance of the additional phase, no complete phase transition has been observed. Moreover, impurity phases like CoO , La_2O_3 and CuO are absent. The La_2CuO_4 and LaCoO_3 compounds have been indexed according to JCPDS card No. 82-0169 and 48-0123 with the *Cmca* and *R3c* space group, respectively. The intensity of the peaks corresponding to the rhombohedral phase gradually increases with increasing Co^{2+} content and dominated the LCC5 sample due to the stable LaCoO_3 secondary phase (Fig. 4). As the Co^{2+} doping concentration is further increased, this effect was found to be more pronounced, and the formation of a stable two-phase perovskite system is confirmed.

The lattice parameters of the orthorhombic/rhombohedral perovskite nanocomposites have been calculated from the X-ray diffraction data using eqn (2) and (3)

$$\frac{1}{d^2} = \frac{h^2}{a^2} + \frac{k^2}{b^2} + \frac{l^2}{c^2} \quad (2)$$

$$\frac{1}{d^2} = \frac{(h^2+k^2+l^2) \sin^2 \alpha + 2(hk+kl+hl)(\cos^2 \alpha - \cos \alpha)}{a^2(1 - 3 \cos^2 \alpha + 2 \cos^3 \alpha)} \quad (3)$$

where d is the inter-atomic spacing, a , b and c are the lattice constants and α is the diffraction angle. The calculated lattice

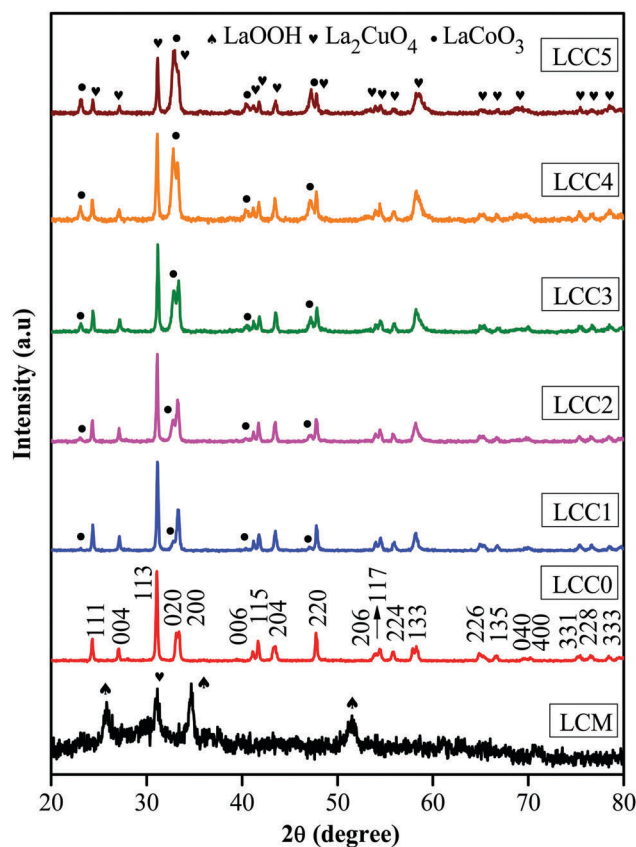


Fig. 3 X-ray diffraction patterns of the $\text{La}_2\text{CuO}_4/\text{LaCoO}_3$ perovskite nanocomposites.

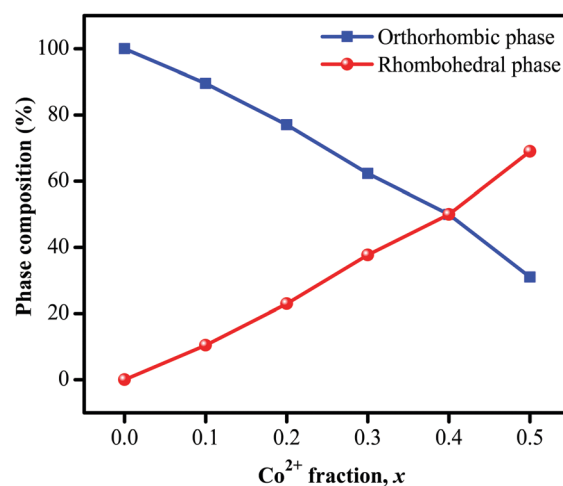


Fig. 4 Phase composition (%) of the $\text{La}_2\text{CuO}_4/\text{LaCoO}_3$ perovskite nanocomposites.

parameters a , b and c as well as the unit cell volume (V) of both the orthorhombic and rhombohedral perovskite phases are illustrated in Table 1.

The variation in the lattice parameters (see Table 1) is attributed to the dissolution of Co^{2+} within the La_2CuO_4 host lattice by occupying La^{3+} sites since both ions have different ionic radii (0.9 Å and 1.36 Å for Co^{2+} and La^{3+} , respectively), in

Table 1 Rietveld refined XRD parameters of the La₂CuO₄/LaCoO₃ perovskite nanocomposites

Sample code	Phase composition %	Crystal structure	Space group	Crystallite size <i>D</i> (nm) ^a	Microstrain	Lattice parameter (Å)	Cell volume (Å ³)	Fit parameters (%)
LCC0	La ₂ CuO ₄	100	Orthorhombic	<i>Bmab</i>	39.6	0.045	<i>a</i> = 5.3589, <i>b</i> = 5.3959, <i>c</i> = 13.1525	380.31 <i>R</i> _{wp} = 13.86 <i>S</i> = 1.20 <i>R</i> _p = 10.36 <i>χ</i> ² = 1.45 <i>R</i> _e = 11.50
LCC1	La ₂ CuO ₄	89.5	Orthorhombic	<i>Cmab</i>	46	0.097	<i>a</i> = 5.3676, <i>b</i> = 13.1340, <i>c</i> = 5.3907	380.03 <i>R</i> _{wp} = 13.46 <i>S</i> = 1.00 <i>R</i> _p = 9.93 <i>χ</i> ² = 1.11 <i>R</i> _e = 12.76
	LaCoO ₃	10.5	Rhombohedral	<i>R</i> $\bar{3}c$	25	0.210	<i>a</i> = 5.4680, <i>c</i> = 13.2620	343.39
LCC2	La ₂ CuO ₄	77	Orthorhombic	<i>Cmab</i>	44.6	0.073	<i>a</i> = 5.3663, <i>b</i> = 13.1320, <i>c</i> = 5.3891	379.77 <i>R</i> _{wp} = 14.44 <i>S</i> = 1.10 <i>R</i> _p = 10.82 <i>χ</i> ² = 1.21 <i>R</i> _e = 13.09
	LaCoO ₃	23	Rhombohedral	<i>R</i> $\bar{3}c$	21	0.260	<i>a</i> = 5.4650, <i>c</i> = 13.2470	342.63
LCC3	La ₂ CuO ₄	62.3	Orthorhombic	<i>Cmab</i>	45	0.138	<i>a</i> = 5.3702, <i>b</i> = 13.1300, <i>c</i> = 5.3860	379.77 <i>R</i> _{wp} = 15.94 <i>S</i> = 1.19 <i>R</i> _p = 11.83 <i>χ</i> ² = 1.43 <i>R</i> _e = 12.90
	LaCoO ₃	37.7	Rhombohedral	<i>R</i> $\bar{3}c$	49	0.520	<i>a</i> = 5.4670, <i>c</i> = 13.2580	343.16
LCC4	La ₂ CuO ₄	50	Orthorhombic	<i>Cmab</i>	36	0.070	<i>a</i> = 5.3705, <i>b</i> = 13.1360, <i>c</i> = 5.3880	380.10 <i>R</i> _{wp} = 14.84 <i>S</i> = 1.07 <i>R</i> _p = 11.15 <i>χ</i> ² = 1.16 <i>R</i> _e = 13.74
	LaCoO ₃	50	Rhombohedral	<i>R</i> $\bar{3}c$	36	0.590	<i>a</i> = 5.4660, <i>c</i> = 13.2460	342.73
LCC5	La ₂ CuO ₄	31	Orthorhombic	<i>Cmab</i>	43	0.740	<i>a</i> = 5.3985, <i>b</i> = 13.1550, <i>c</i> = 5.3739	381.63 <i>R</i> _{wp} = 17.17 <i>S</i> = 1.24 <i>R</i> _p = 13.61 <i>χ</i> ² = 1.54 <i>R</i> _e = 13.80
	LaCoO ₃	69	Rhombohedral	<i>R</i> $\bar{3}c$	45	0.660	<i>a</i> = 5.4310, <i>c</i> = 13.4260	342.95

^a Average crystallite size *D* (nm) by Debye–Scherrer's formula.

addition to the effect of cation concentration in a solid solution by the miscibility limit of the corresponding phase formation.⁴¹

The average crystallite size (*D*) of the orthorhombic/rhombohedral perovskite nanocomposites has been calculated using the Debye–Scherrer formula:³⁸

$$D = \frac{0.89\lambda}{\beta \cos \theta} \quad (4)$$

where, λ is the X-ray wavelength, θ is the Bragg diffraction angle and β is the full width at half maximum (FWHM). Table 1 indicates an average crystallite size for the undoped La₂CuO₄ of about 39.6 nm. The Co²⁺ doped La₂CuO₄ (orthorhombic) and LaCoO₃ (rhombohedral) possessed a crystallite size in the range of 36–46 nm and 21–49 nm, respectively. The obtained changes in the values of the crystallite size in both La₂CuO₄ and LaCoO₃ phases can be associated with experimental factors such as the concentration of Co²⁺ dopant and intrinsic parameters such as the nature of the dopant and the type of crystal structure, for instance orthorhombic and rhombohedral, due to the effect of atomic arrangements on grain growth (preferred orientation during grain growth occurs along the facile direction that is energetically favorable).

Fig. 5 shows the Rietveld refinements performed on the La₂CuO₄/LaCoO₃ perovskite nanocomposites using PDXL software. The refinements were carried out to confirm two phase formation. The observed X-ray diffraction patterns of the La₂CuO₄/LaCoO₃ composites match well with the calculated ones (Fig. 5), as the values of χ^2 given in Table 1 are closer to 1.

The goodness of fit parameter (*S*) was calculated from $S = R_{wp}/R_e$, where *R*_{wp} is the weighted profile and *R*_e is the expected weighted profile reliability factor, respectively. The value of 'S' around unity indicates the excellent goodness of fit and confirms that the refined parameters are determined more precisely.⁴²

3.3. FTIR analysis

Fig. 6 shows the FTIR spectra of the La₂CuO₄/LaCoO₃ perovskite nanocomposites. The broad band centered at about 3747 cm⁻¹ can be associated with the O–H longitudinal stretching vibration of the adsorbed water molecules, while the adsorption bands at 1732 and 1530 cm⁻¹ are ascribed to the H–O–H vibration. The weak band at 1380 cm⁻¹ may be assigned to the residual nitrogen group due to the combustion process. In addition, the two high intensity bands at 682 and 512 cm⁻¹ are correlated to the La–O and Cu–O stretching modes of the orthorhombic La₂CuO₄ phase.⁴³ The LCC5 sample with a maximum amount of LaCoO₃ and a minimum amount of the La₂CuO₄ phase (Fig. 4), shows the stretching vibrations at 580 and 445 cm⁻¹, which are characteristic bands of the LaCoO₃ perovskite phase.³⁰ The steady decrease of the band intensity at 682 and 512 cm⁻¹ is due to the decrease in the amount of the orthorhombic phase alongside the increase in the amount of the rhombohedral phase with increasing Co²⁺ doping fraction.

3.4. Optical properties

The optical properties of the Co²⁺ doped La₂CuO₄/LaCoO₃ perovskite nanocomposites were studied using UV-Vis diffuse

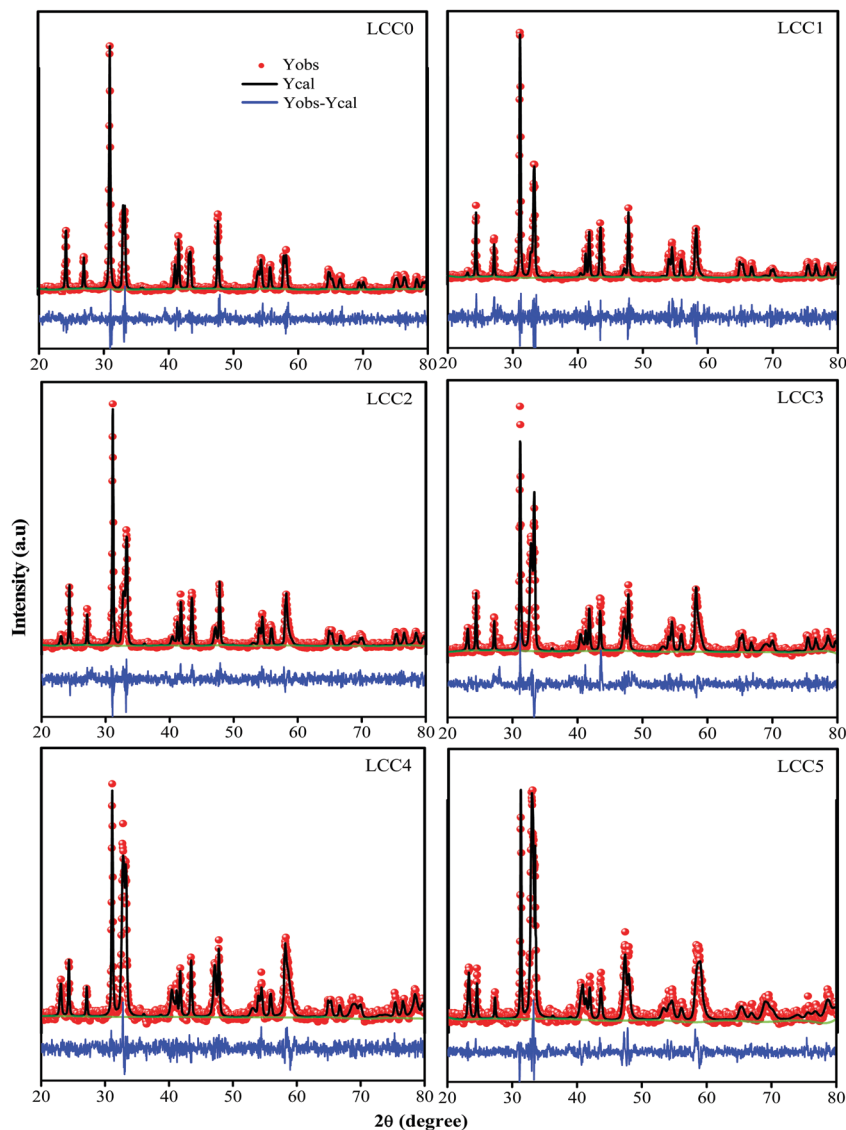


Fig. 5 Rietveld refined XRD patterns for the $\text{La}_2\text{CuO}_4/\text{LaCoO}_3$ perovskite nanocomposites.

reflectance spectroscopy. The Kubelka–Munk (K–M) function $[F(R)]$ is generally applied to convert the diffuse reflectance into the equivalent absorption coefficient (α) as given in eqn (5) and mostly used for analyzing the powder samples:³⁸

$$\alpha = F(R) = \frac{(1 - R)^2}{2R} \quad (5)$$

where, $F(R)$ is the K–M function, α is the absorption coefficient and R is the reflectance. Thus the Tauc relation becomes:

$$F(R)h\nu = A(h\nu - E_g)^n \quad (6)$$

where $n = 1/2$ and 2 for direct and indirect transitions, respectively, thereby giving direct and indirect band gaps. The $(F(R)h\nu)^2$ versus $h\nu$ plots are shown in Fig. 7. The extrapolation of the linear region to $(F(R)h\nu)^2 = 0$ gives the band gap value. The optical band gap value of the undoped La_2CuO_4 perovskite is 1.88 eV, which is higher than the reported values of 1.30 eV and 1.24 eV.^{8,44}

This may be due to quantum confinement phenomena occurring at the nano-regime. With Co^{2+} doping, two linear regions are observed corresponding to the La_2CuO_4 and LaCoO_3 perovskite phases. The optical band gap of the pure LaCoO_3 perovskite is 3.09 eV.²⁴ With increasing Co^{2+} content, the band gap related to the first region corresponding to the orthorhombic phase increases from 2.32 eV to 2.56 eV and that of the rhombohedral phase increases from 2.94 eV to 3.09 eV (Table 2). The increase in the bulk band gap for the $\text{La}_2\text{CuO}_4/\text{LaCoO}_3$ nanocomposite may be due to the Co^{2+} substitution effect. This is due to an increase in bond-mismatch, which is the variation of the lattice parameters a , b and c . The substitution of La^{3+} (large radii) by Co^{2+} (small radii) within the La_2CuO_4 host lattice will enhance the bond mismatch by contracting the $(\text{LaO})_2$ layers. This will lead to the expansion of CuO_2 and CoO_6 sheets, resulting in an increase in the band gap of the La_2CuO_4 and LaCoO_3 perovskite phases, respectively.⁸

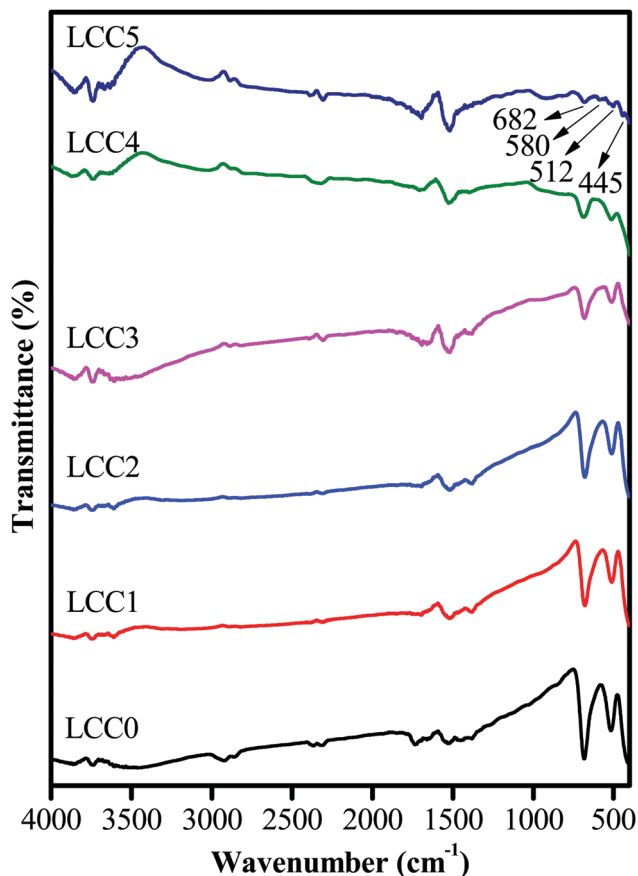


Fig. 6 FT-IR spectra of the $\text{La}_2\text{CuO}_4/\text{LaCoO}_3$ perovskite nanocomposites.

3.5. SEM and EDX studies

The HR-SEM micrographs of the $\text{La}_2\text{CuO}_4/\text{LaCoO}_3$ nanocomposites shown in Fig. 8 reveal the intragranular pores while the pore walls are fused grains with distinct grain boundaries. Moreover, with increasing Co^{2+} concentration, the intragranular porosity increases while larger grains are reduced to small. The particle sizes estimated from the HR-SEM images of the $\text{La}_2\text{CuO}_4/\text{LaCoO}_3$ perovskite nanocomposites gradually decrease from 87 to 37 nm. The particle size as seen from the SEM images is slightly different from the crystallite size obtained by XRD analysis, because the former is associated with aggregated cluster size, while the latter is associated with the diffracting domain size in the nanoparticle.⁴⁵ EDX (Fig. 9) analysis was used to examine the elemental composition of the $\text{La}_2\text{CuO}_4/\text{LaCoO}_3$ perovskite nanocomposites and confirmed the presence of La/Co, Cu and O elements and the inset table shows the respective fraction of the elemental composition.

3.6. Magnetic properties

Fig. 10 illustrates the magnetisation–field (M – H) hysteresis curves of the $\text{La}_2\text{CuO}_4/\text{LaCoO}_3$ perovskite nanocomposites recorded at room temperature under a 1 Tesla magnetic field. For the un-doped LCC0 sample, only ferro-/para-magnetic behaviour is observed; the corresponding saturation magnetization (M_s)

is $2.547/3.528 \text{ memu g}^{-1}$ (obtained after the removal of the paramagnetic component by using the MicroMag software). LaCoO_3 is a nonmagnetic insulator at the ground state with a paramagnetic insulating state developing at a low temperature of about 50 K, and at around 500 K an insulator-to-metal transition is observed.⁴⁶ As shown in Fig. 4, with increasing Co^{2+} content $0.1 \leq x \leq 0.3$ (LCC1 to LCC3 samples), the amount of La_2CuO_4 decreases (from 89.5 to 62.3%); meanwhile, the LaCoO_3 amount increases (from 10.5 to 37.7%). So obviously a para-/ferro-magnetic transition occurs; the nanocomposites present a dominant paramagnetic component alongside a small ferromagnetic phase and the corresponding bulk magnetisation at maximum field gradually increases from 18.91 to $31.12 \text{ memu g}^{-1}$. Furthermore, at a higher Co^{2+} content; *i.e.* $x = 0.4$ (LCC4) and 0.5 (LCC5), the amount of the secondary LaCoO_3 phase becomes more important; 50 and 69% at the expense of La_2CuO_4 reaching 50 and 31%. The corresponding nanocomposites become totally paramagnetic and this can be explained as follow: (i) the substitution of La ($2.5 \mu_B$) by Co with higher moment ($3.5\text{--}5.0 \mu_B$) will reinforce the magnetic ordering not the magnetic transformation from para-ferro; in this case, the bulk magnetization increases with increasing Co^{2+} content as shown in Table 2 and Fig. 10; (ii) the LaCoO_3 phase is known to be paramagnetic at room temperature,⁴⁷ thereby the higher its amount, the more the bulk nanocomposite becomes paramagnetic; (iii) Co^{2+} may occupy the non-magnetic Cu^{2+} sites instead of La^{3+} sites, and thereby result as well in reinforcing the bulk magnetic moment. Herein, it should be highlighted that the main objective of the present work is to substitute La^{3+} by Co^{2+} within the La_2CuO_4 phase. However, the crystallization of the La_2CuO_4 phase from the solution containing La^{3+} , Cu^{2+} , and Co^{2+} formed from the starting precursors, and Co^{2+} may also occupy the Cu^{2+} sites within La_2CuO_4 because they have close ionic radii compared to La^{3+} . By suggesting so, all possibilities that may occur during the synthesis are taken into consideration, in order to explain the change in the magnetic behavior and properties. The value of bulk magnetisation at the maximum field of LCC4 and LCC5 increases 41.51 and $47.71 \text{ memu g}^{-1}$, meanwhile, the value of (M_s) for the ferromagnetic phase remains low in the $1.9\text{--}3.5 \text{ memu g}^{-1}$ range (Table 2). The as-obtained modifications in the magnetic properties can be associated most probably with the exchange of A and B sites within the La_2CuO_4 host lattice because of Co^{2+} doping; as well as the important phase composition of $\text{La}_2\text{CuO}_4/\text{LaCoO}_3$ obtained from the ferromagnetic-to-paramagnetic transition. The formation of the paramagnetic perovskite LaCoO_3 phase and the increase of its amount with increasing Co^{2+} doping content, reinforce the paramagnetic phase at the expense of the ferromagnetic phase. In a composite, the bulk properties represent a combination of individual properties of its constituents. The bulk magnetization value has suddenly changed at a certain Co^{2+} doping content, due to the transition between single domain and multi-domain at the critical size.⁴⁸

Since the relative difference in the ionic radii of La^{3+} (1.36 \AA) and Co^{2+} (0.9 \AA)⁴⁹ is significant, the substituted ions give rise to a ‘distorted’ perovskite structure,⁴⁶ resulting in the creation of some point defects (vacancies or interstitials). For the moment, the 2^+ state of Co and the 3^+ state of La, this means that the

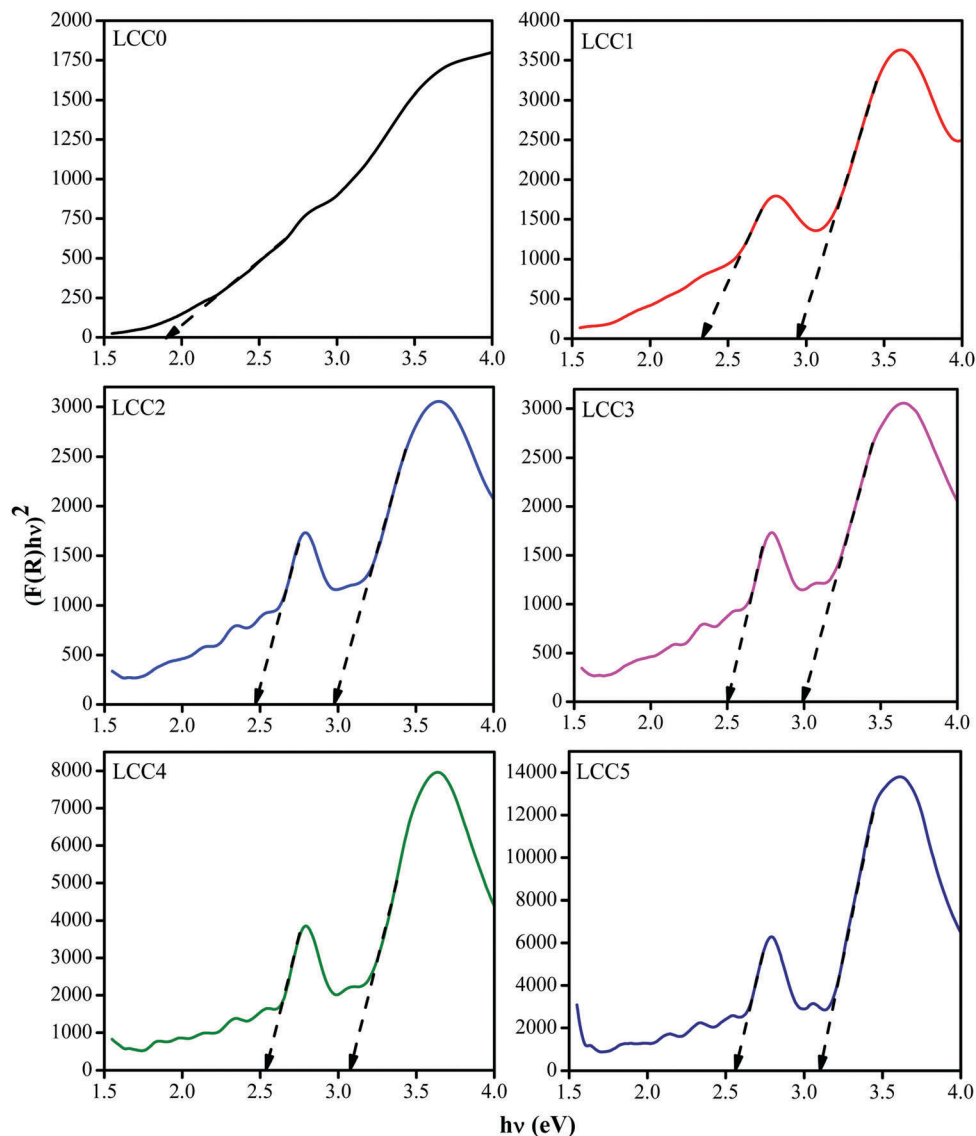


Fig. 7 Plot of $(F(R)h\nu)^2$ versus $h\nu$ for the $\text{La}_2\text{CuO}_4/\text{LaCoO}_3$ perovskite nanocomposites.

Table 2 Magnetic properties and bandgap of the $\text{La}_2\text{CuO}_4/\text{LaCoO}_3$ perovskite nanocomposites

Sample code	Magnetic behavior	Coercivity H_c (Oe)	Remanence M_r ($\mu\text{emu g}^{-1}$)	Saturation magnetisation M_s , (memu g^{-1})	Bandgap E_g (eV)	
					Orthorhombic	Rhombohedral
LCC0	Ferro Para	542.3 519.9	910.6 910.6	2.547 3.528 ^a	1.88	—
LCC1	Para/Ferro Ferro	102.8 177.27	724.1 724.1	18.91 ^a 3.12	2.32	2.94
LCC2	Para/Ferro Ferro	9.465 14.43	5.447 21.00	22.02 ^a 1.92	2.49	2.96
LCC3	Para/Ferro Ferro	24.89 29.60	208.8 208.8	31.12 ^a 3.51	2.51	2.99
LCC4	Para	7.030	59.81	41.51 ^a	2.53	3.06
LCC5	Para	24.08	129.1	47.71 ^a	2.56	3.09

^a Magnetization at the maximum field of 1 T.

substitution of La^{3+} by Co^{2+} will result in unbalanced total charge of the compound (positive charge), which will create some oxygen vacancies. However, the real situation may be a bit

complex, as direct/indirect combined effects may occur simultaneously, together with the creation of defects; the replacement of the 4f rare earth element La^{3+} with weak

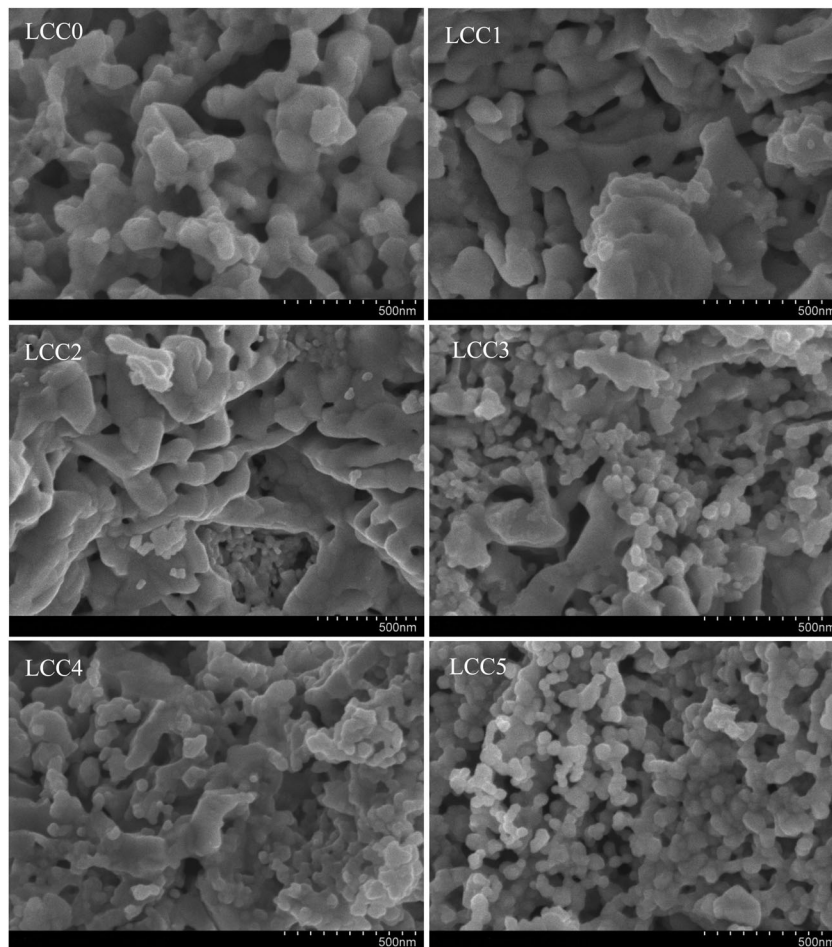


Fig. 8 HR-SEM images of the $\text{La}_2\text{CuO}_4/\text{LaCoO}_3$ perovskite nanocomposites.

paramagnetic behaviour by the 3d transition metal Co^{2+} having a paramagnetic behaviour, and short/long exchange interactions between various La^{3+} , Co^{2+} , Cu^{2+} and O^{2-} ions.

3.7. Nitrogen adsorption/desorption isotherms

The surface area has been determined from the N_2 adsorption-desorption isotherms, recorded at 77 K using the BET technique as shown in Fig. 11. All samples exhibit a mixture of type II and type IV isotherms, according to the IUPAC classification. The hysteresis loops observed in the high P/P_0 range indicate the formation of mesopores in the $\text{La}_2\text{CuO}_4/\text{LaCoO}_3$ perovskite nanocomposites. The surface area (S_{BET}), pore diameter (D_p) and pore volume (V_p) are given in Table 3. The BET surface area of pure undoped La_2CuO_4 was found to be $12.2 \text{ m}^2 \text{ g}^{-1}$. However, increasing the Co^{2+} doping fraction results in a gradual increase of the surface area upto $43.7 \text{ m}^2 \text{ g}^{-1}$ for the LCC5 sample.

Except for the LCC2 sample, all other samples possess an average pore diameter between 3.3 and 3.7 nm, indicating the presence of mesopores. In LCC2, the steepness of the isotherms is observed at a high relative pressure ($P/P_0 > 0.78$). This could be due to the presence of uniform cylindrical pores and ordered three dimensional pore networks. In this case, the adsorption

process would be associated with the delayed condensation of the adsorbate while the desorption would be associated with the equilibrium vapor-liquid transition leading to a non-comparable behavior in the pore diameter (D_p) and pore volume (V_p) values for the LCC2 sample.^{50,51} Thus, the results of surface area, pore size and pore volume indicate that the $\text{La}_2\text{CuO}_4/\text{LaCoO}_3$ perovskite nanocomposite system possesses appropriate porosity and surface area suitable for catalytic applications.

3.8. Catalytic activities of $\text{La}_2\text{CuO}_4/\text{LaCoO}_3$ perovskite nanocomposites

The $\text{La}_2\text{CuO}_4/\text{LaCoO}_3$ perovskite nanocomposites have been tested for the oxidation of glycerol in a liquid phase batch reactor under atmospheric conditions. For undoped La_2CuO_4 , the conversion of glycerol was found to be 80% with a selectivity of 91%. Furthermore, upon doping with Co^{2+} ($0.1 \leq x \leq 0.5$), the conversion of glycerol increases from 83.3% to 96.5% and the selectivity of formic acid (as observed for GC-MS results shown in Fig. 12) increases also from 79.8% to 95.1%. The LCC5 catalyst yielded the highest catalytic activity for the conversion of glycerol to formic acid as shown in Table 4. Therefore, the LCC5 sample was used for further optimization studies.

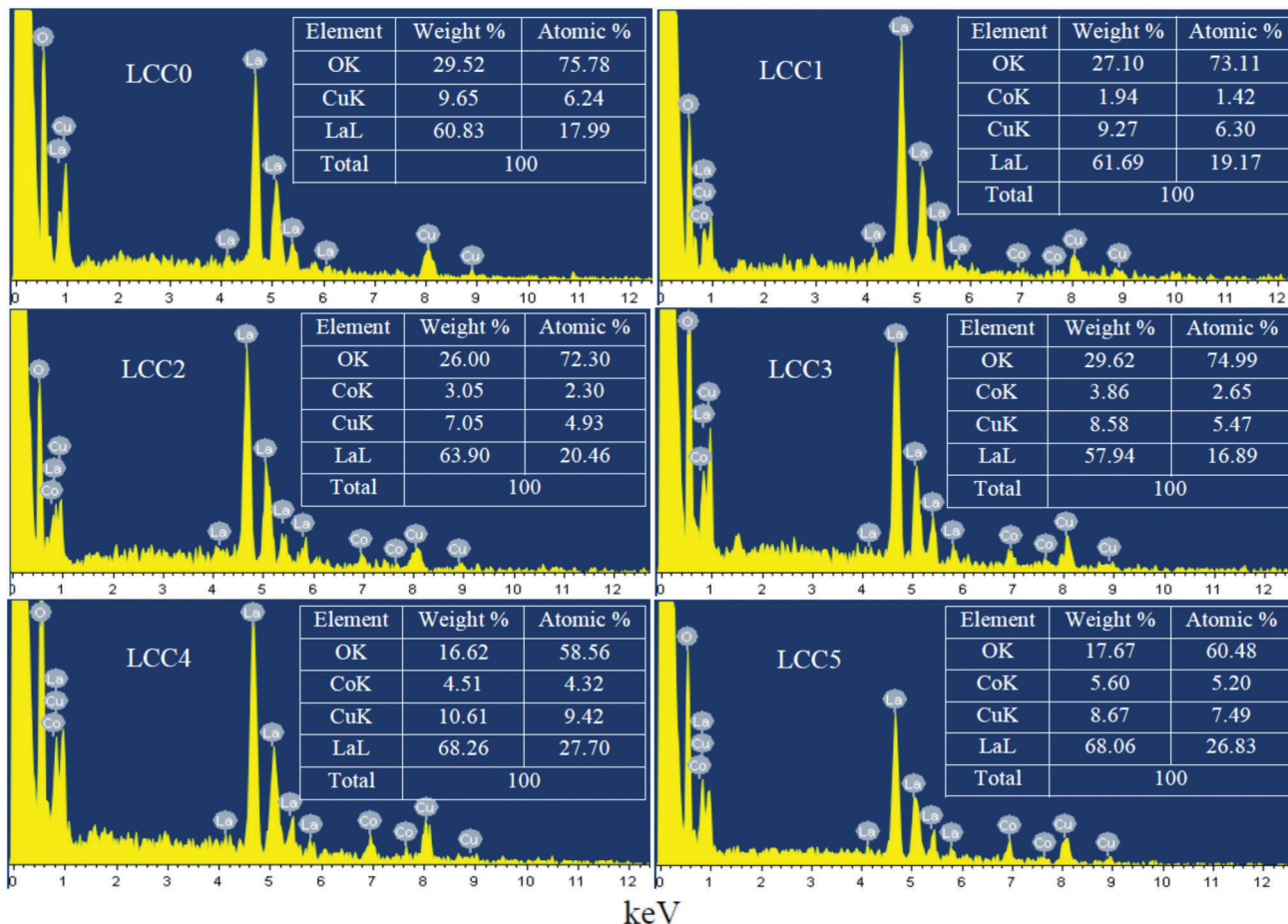


Fig. 9 EDX spectra of the $\text{La}_2\text{CuO}_4/\text{LaCoO}_3$ perovskite nanocomposites.

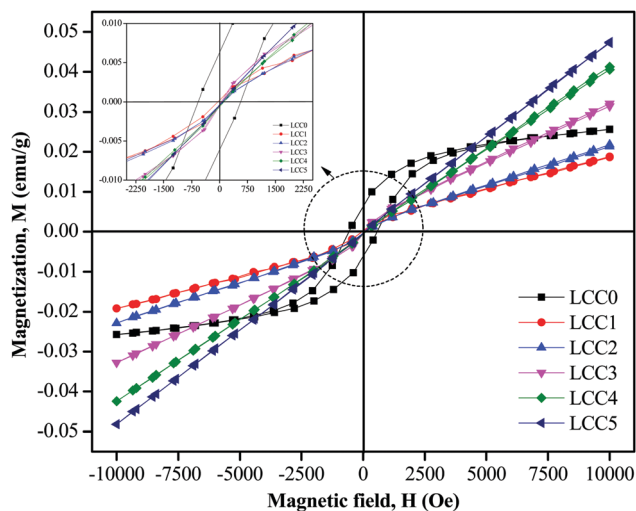


Fig. 10 Magnetic hysteresis curves of the $\text{La}_2\text{CuO}_4/\text{LaCoO}_3$ perovskite nanocomposites.

3.9. Effect of composite loading

The catalytic conversion of glycerol and the selectivity over the LCC5 nanocomposite catalyst at 70 °C for 6 h with different composite loadings (10 to 70 mg) are shown in Fig. 13. It can be

noticed that the conversion of glycerol increases from 76.3% to 98.9%; meanwhile, the selectivity of formic acid increases from 87.4% to 95.1% for 10 to 50 mg of the catalyst and thereafter decreases to 89.1% for a higher loading of 70 mg. The reduction in the selectivity of formic acid beyond 50 mg of the composite may be due to the pore blocking of the catalyst surface, which led to a decline or decrease in the reactive surface area available to proceed the reaction.⁵²

3.10. Recycling test

The reusability of the LCC5 nanocomposite catalyst for the conversion of glycerol has also been investigated. After the first reaction, the catalyst was filtered and washed with distilled water several times, then dried at 150 °C for 2 h and reused for another four catalytic runs. The results reveal (Fig. 14) a slight decrease in the conversion of glycerol and the selectivity of formic acid, but both values remain around 90%. This can be attributed to the mass loss during the catalyst washing and recovery process.⁵³

3.11. Reaction pathway

The proposed mechanism of glycerol oxidation to produce formic acid is shown in Scheme 1. It is a sequential reaction that follows two paths. The first pathway involves the oxidation

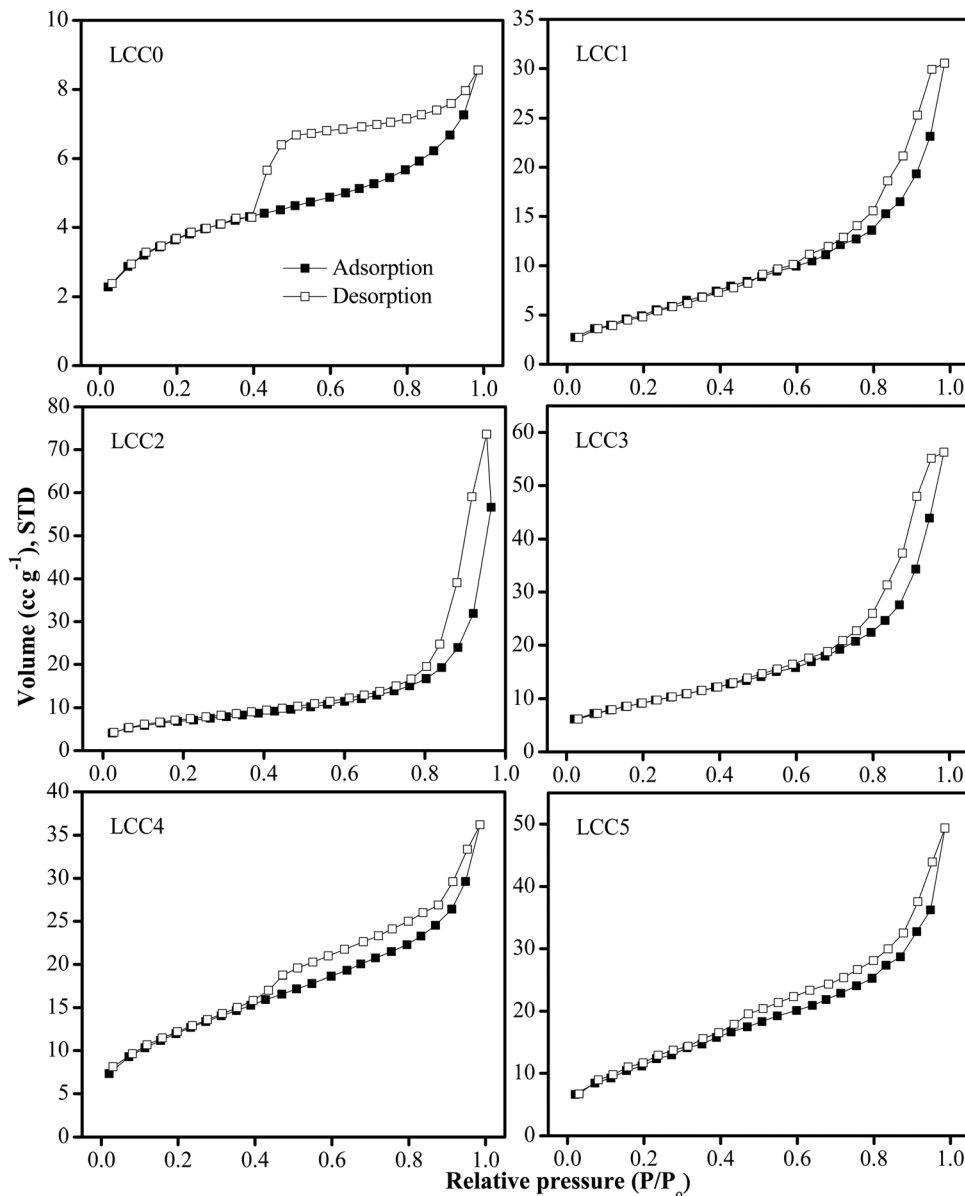


Fig. 11 N_2 adsorption–desorption isotherms obtained from the BET measurements of the $La_2CuO_4/LaCoO_3$ perovskite nanocomposites.

Table 3 BET surface area, pore diameter and pore volume of the $La_2CuO_4/LaCoO_3$ perovskite nanocomposites

Sample code	Surface area, S_{BET} ($m^2 g^{-1}$)	Pore diameter, D_p (d) (nm)	Pore volume, V_p ($cc g^{-1}$)
LCC0	12.2	3.3	0.013
LCC1	20.4	3.6	0.049
LCC2	24.2	1.2	0.118
LCC3	33.5	3.6	0.053
LCC4	42.6	3.6	0.057
LCC5	43.7	3.7	0.086

of glycerol with an initial loss of terminal hydroxyl groups to form enol, which readily forms acetol (hydroxyacetone) by tautomerism. This is followed by a radical fragmentation related to a Norrish type I process (which would undergo rapid

C–C bond cleavage) to form acetaldehyde and methanol precursors, which on reduction lead to acetaldehyde and methanol. Acetaldehyde is later oxidized to form acetic acid. On the other hand, methanol is oxidized (loss of hydrogen radical) to form formaldehyde, which later gets oxidized to form formic acid.⁵⁴ The second reaction pathway involves the oxidation of glycerol to form glyceraldehyde, which is then oxidized to glyceric acid. It would undergo rapid C–C bond cleavage to form glycolic acid and formaldehyde, where the latter is readily oxidized to form formic acid.⁵⁵

A literature survey has been carried out in order to gain insight into the results that were obtained. Nevertheless, it is clearly highlighted that it is very difficult to make a conclusive comparison with the literature, since in this study, we obtained a nanocomposite system formed by the two perovskite phases

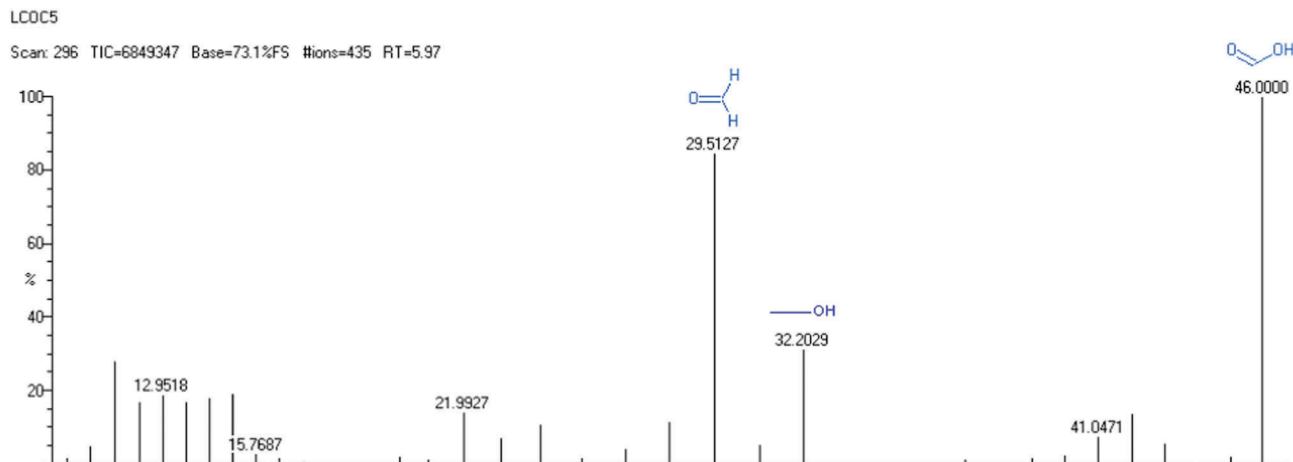


Fig. 12 GC-MS spectra of glycerol oxidation using the LCC5 perovskite sample.

Table 4 Effect of Co^{2+} doping on the conversion of glycerol and selectivity

Sample code	Glycerol conversions (%)	Selectivity of formic acid (%)
LCC0	80.0	91.0
LCC1	83.3	79.8
LCC2	86.8	83.6
LCC3	90.2	87.3
LCC4	93.4	90.5
LCC5	96.5	95.1

Reaction conditions: 50 mmol of (glycerol, H_2O_2 and DMSO), catalyst 50 mg, reaction time 6 h and temperature 70°C .

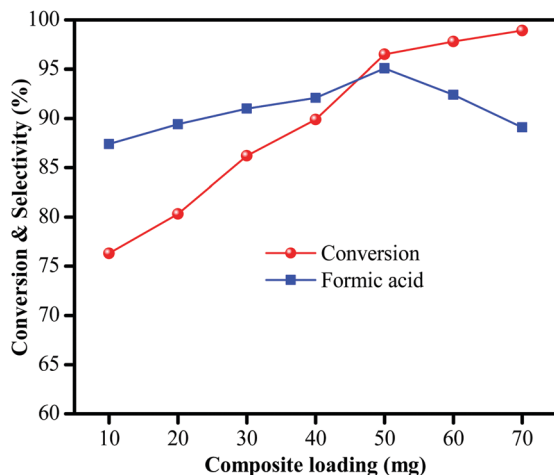


Fig. 13 Effect of composite loading on the conversion of glycerol over the LCC5 sample.

La_2CuO_4 and LaCoO_3 making heterojunctions, resulting in novel bulk properties compared to the individual and different properties of each phase (crystal structure, amount, crystallite size, site occupancy, doping, presence of vacancies, etc.).

Shin-ichi Uchida *et al.* showed that this La_2CuO_4 perovskite compound is paramagnetic with small susceptibility $\sim 10^{-7}$ emu g^{-1} over a wide temperature range (0–300 K) with

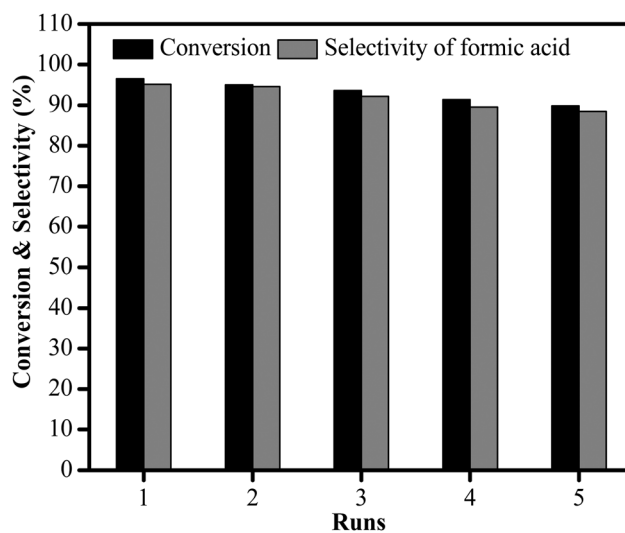
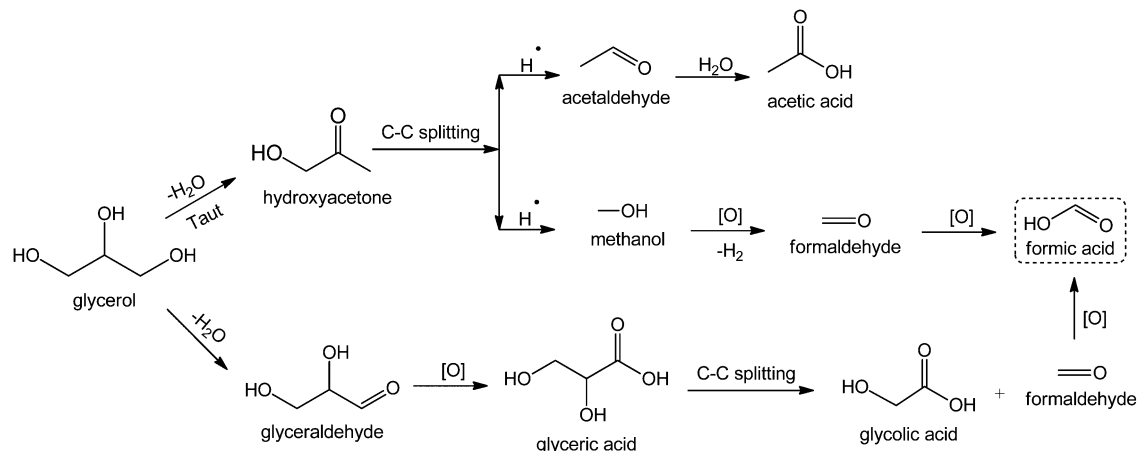


Fig. 14 Recycling performance of the LCC5 sample.

the appearance of a cusp at 250 K. From DFT calculations, it has been reported that $\text{La}_2\text{CuO}_{4+\delta}$ (presence of interstitial oxygen O_i) and Sr-doped La_2CuO_4 have anti-ferromagnetic (AFM) behavior.^{56,57} Meanwhile, even though LaCoO_3 is known as diamagnetic, both experimental and DFT calculations indicated the following: (i) Andrew M. Ritzmann *et al.*⁵⁸ studied the influence of the spin state of Co^{3+} on the oxygen transport in LaCoO_3 and showed that low spin (LS) Co^{3+} promotes higher oxygen vacancy concentrations; (ii) while Dechao Menget *et al.*⁵⁹ revealed that ferromagnetism (FM) can be achieved. This can be originated from the high concentration of high spin (HS) Co^{3+} , and FM coupling between the nearest HS Co^{3+} and LS Co^{3+} . However, when oxygen vacancies (O_v) are created, the FM is suppressed. To the knowledge of the authors, only one perovskite-perovskite system reported by Liang Qiao *et al.*⁶⁰ showed that epitaxial $\text{LaCoO}_3/\text{SrTiO}_3$ (inorganic/inorganic) heterostructures revealed ferromagnetic order at a low temperature (5 K) associated with dimensionality controlled octahedral symmetry-mismatch.



Scheme 1 Proposed mechanism of glycerol oxidation to formic acid.

From several studies reported in the literature, it can be noticed that the magnetic behavior of un-doped and doped perovskite phases, for instance La_2CuO_4 and LaCoO_3 , is somehow complicated. Both experimental and theoretical results indicated that numerous parameters may have a direct or a combined influence on the evolution of their physical properties (magnetic, catalytic, *etc.*), including but not limited to: (i) nature of the doping element and its content either on A (La) or/and B (Co, Cu) sites; (ii) spin state of B ions (low, intermediate and high spin) and interaction between the different spin states; (iii) the presence of oxygen vacancies (O_v) and interstitials (O_i) and their interaction with their environment within the host lattice; and so on. Herein, it is essential to mention that figuring out the properties of a composite starting from individual phase properties is not straightforward; as the complex combination of several factors may interfere simultaneously.

Interestingly, in this study the formation of a perovskite-type $\text{La}_2\text{CuO}_4/\text{LaCoO}_3$ (orthorhombic/rhombohedral) heterointerface nanocomposite with controllable phase composition through the substitution of La by Co, results in interesting properties: (i) tunable energy bandgap (1.88–2.56 eV for La_2CuO_4 and 2.94–3.09 eV for LaCoO_3); the appearance of ferromagnetic order with saturation magnetization influenced by the Co^{2+} content alongside with a ferro–para transition; and high catalytic properties (glycerol conversion in the 80–96% range). The as-obtained results may be associated with combined effects mainly but not limited to quantum confinement at the nanoscale; complex site occupancy in both phases (Co^{2+} from the precursor may occupy La^{3+} or Cu^{2+} sites within La_2CuO_4); the presence of grain boundaries, which favor/facilitate oxygen transport and thereby the creation of oxygen vacancies/interstitials; and the oxidation of Co^{2+} (starting precursor) to Co^{3+} (favoring the formation of LaCoO_3) in a complex process in addition to the interaction between HS–LS of Co^{2+} (1.73 and 3.88 μ_B) affecting the magnetic order and total magnetization.

Thus the as-fabricated heterointerface of the $\text{La}_2\text{CuO}_4/\text{LaCoO}_3$ composite system with better control of the electronic properties and thereby the corresponding structural modifications has resulted in the development of a novel magnetically functional material to be employed for catalytic applications.

4. Conclusions

$\text{La}_2\text{CuO}_4/\text{LaCoO}_3$ perovskite nanocomposites have been successfully synthesized by a microwave combustion method. The undoped La_2CuO_4 (LCC0) shows a single perovskite phase with orthorhombic structure. Upon doping with Co^{2+} , the formation of $\text{La}_2\text{CuO}_4/\text{LaCoO}_3$ perovskite nanocomposites was observed and further validated by Rietveld refinements. At lower Co^{2+} doping (LCC1), the orthorhombic phase is dominant while at higher Co^{2+} doping, the rhombohedral phase becomes dominant (LCC5). The average crystallite size of the nanocomposites varies in a narrow range, *i.e.* 36–46 nm and 21–49 nm for the orthorhombic and rhombohedral phases, respectively. FT-IR analysis confirms the vibrational stretching modes of the $\text{La}_2\text{CuO}_4/\text{LaCoO}_3$ perovskites. The optical band gap value of the orthorhombic/rhombohedral phases increases with an increase in the Co^{2+} content. Morphological observations reveal a well developed intragranular porosity with distinct grains on the surfaces. Magnetic measurements indicate the appearance of ferro-/para-magnetic behaviour. The textural properties of the $\text{La}_2\text{CuO}_4/\text{LaCoO}_3$ perovskite nanocomposite show an extent of mesoporosity with a maximum BET surface area of 43.7 $\text{m}^2 \text{g}^{-1}$. $\text{La}_2\text{CuO}_4/\text{LaCoO}_3$ perovskites behave as a potential catalyst for the selective liquid phase oxidation of glycerol to formic acid, exhibiting high conversion and selectivity above 95%.

Conflicts of interest

There are no conflicts to declare.

References

- 1 T. Prakash, G. V. M. Williams, J. Kennedy and S. Rubanov, *J. Appl. Phys.*, 2016, **120**, 123905.
- 2 J. Kennedy, G. V. M. Williams, P. P. Murmu and B. J. Ruck, *Phys. Rev. B: Condens. Matter Mater. Phys.*, 2013, **88**, 214423.
- 3 P. P. Murmu, J. Kennedy, G. V. M. Williams, B. J. Ruck, S. Granville and S. V. Chong, *Appl. Phys. Lett.*, 2012, **101**, 082408.

- 4 G. V. M. Williams, T. Prakash, J. Kennedy and S. V. Chong, *J. Magn. Magn. Mater.*, 2018, **460**, 229–233.
- 5 K. Kaviyarasu, P. P. Murmu, J. Kennedy, F. T. Thema, D. Letsholathebe, L. Kotsedi and M. Maaza, *Nucl. Instrum. Methods Phys. Res., Sect. B*, 2017, **409**, 147–152.
- 6 M. Napoletano, J. M. G. Amores, E. Magnone, G. Busca and M. Ferretti, *Phys. C*, 1999, **319**, 229–237.
- 7 T. Uchiyama, R. Karita, M. Nishibori, H. Einaga and Y. Teraoka, *Catal. Today*, 2015, **251**, 7–13.
- 8 Y. Li, J. Huang, L. Cao, J. Wu and J. Fei, *Mater. Charact.*, 2012, **64**, 36–42.
- 9 J. Zhu, Z. Zhao, D. Xiao, J. Li, X. Yang and Y. Wu, *Mater. Chem. Phys.*, 2005, **94**, 257–260.
- 10 A. Tavana, M. Akhavan and C. Draxl, *Phys. C*, 2015, **517**, 20–25.
- 11 L. Xu, C. Qin, Y. Wan, H. Xie, Y. Huang, L. Qin and H. Jin, *J. Taiwan Inst. Chem. Eng.*, 2017, **71**, 433–440.
- 12 H. Einaga, Y. Nasu, M. Oda and H. Saito, *Chem. Eng. J.*, 2016, **283**, 97–104.
- 13 M. Ghasdi and H. Alamdari, *Sens. Actuators, B*, 2010, **148**, 478–485.
- 14 A. C. Terracciano, S. T. De Oliveira, S. S. Vasu and N. Orlovskaya, *Exp. Therm. Fluid Sci.*, 2018, **90**, 330–335.
- 15 H. A. R. Aliabad, V. Hesam, I. Ahmad and I. Khan, *Phys. B*, 2013, **410**, 112–119.
- 16 S. Mukhopadhyay, M. W. Finnis and N. M. Harrison, *Phys. Rev. B: Condens. Matter Mater. Phys.*, 2013, **87**, 125132.
- 17 X. Wang, Y. Han, X. Song, W. Liu and H. Cui, *Comput. Mater. Sci.*, 2017, **136**, 191–197.
- 18 G. H. Staab, *Laminar Composites*, Elsevier Inc., 2nd edn, 2015.
- 19 K. Long, X. Du, S. Xu and Y. M. Xie, *Compos. Struct.*, 2016, **153**, 593–600.
- 20 A. Afzaal and M. A. Farrukh, *Mater. Sci. Eng., B*, 2017, **223**, 167–177.
- 21 A. A. Yelwande, M. E. Navgire, D. T. Tayde, B. R. Arbad and M. K. Lande, *Bull. Korean Chem. Soc.*, 2012, **33**, 1856–1860.
- 22 X. Zhou, Q. Cao, Y. Hu, J. Gao and Y. Xu, *Sens. Actuators, B*, 2001, **77**, 443–446.
- 23 X. Chen, K. Tang, S. Zeng, Q. Hao, D. Wang, Z. Gao and Y. Wang, *J. Alloys Compd.*, 2015, **626**, 239–244.
- 24 C. Zhang, H. He, N. Wang, H. Chen and D. Kong, *Ceram. Int.*, 2013, **39**, 3686–3689.
- 25 M. Velasquez, A. Santamaria and C. Batiot-Dupeyrat, *Appl. Catal., B*, 2014, **160–161**, 606–613.
- 26 J. A. Villoria, M. C. Alvarez-Galvan, S. M. Al-Zahrani, P. Palmisano, S. Specchia, V. Specchia, J. L. G. Fierro and R. M. Navarro, *Appl. Catal., B*, 2011, **105**, 276–288.
- 27 L. Gao, X. Wang, H. Tong Chua and S. Kawi, *J. Solid State Chem.*, 2006, **179**, 2036–2040.
- 28 S. Jayapandi, D. Lakshmi, S. Premkumar, P. Packiyaraj and K. Anitha, *Mater. Lett.*, 2018, **218**, 205–208.
- 29 J. Chen, M. Shen, X. Wang, J. Wang, Y. Su and Z. Zhao, *Catal. Commun.*, 2013, **37**, 105–108.
- 30 S. Sun, L. Yang, G. Pang and S. Feng, *Appl. Catal., A*, 2011, **401**, 199–203.
- 31 Q. Tu, X. Chen, B. Ma, Z. Zhao, J. Li and J. Liang, *Phys. C*, 2002, **370**, 94–100.
- 32 J. L. Hueso, A. Caballero, M. Ocaña and A. R. González-Elipe, *J. Catal.*, 2008, **257**, 334–344.
- 33 K. Kaviyarasu, L. Kotsedi, A. Simo, X. Fuku, G. T. Mola, J. Kennedy and M. Maaza, *Appl. Surf. Sci.*, 2017, **421**, 234–239.
- 34 K. Dharmalingam, D. Pamu and R. Anandalakshmi, *Mater. Lett.*, 2018, **212**, 207–210.
- 35 F. Gu, C. Li, Y. Hu and L. Zhang, *J. Cryst. Growth*, 2007, **304**, 369–373.
- 36 S. S. Thinda, C. C. Mustapica, J. Wena, C. D. Goodwinb and A. Chen, *New J. Chem.*, 2017, **41**, 10542–10549.
- 37 K. Natarajan, P. Singh, H. C. Bajaj and R. J. Tayade, *Korean J. Chem. Eng.*, 2016, **33**, 1788–1798.
- 38 G. T. Anand, L. J. Kennedy, J. J. Vijaya, K. Kaviyaran and M. Sukumar, *Ceram. Int.*, 2014, **41**, 603–615.
- 39 G. Theophil Anand, L. John Kennedy, U. Aruldoss and J. Judith Vijaya, *J. Mol. Struct.*, 2015, **1084**, 244–253.
- 40 M. Sukumar and L. J. Kennedy, *J. Nanosci. Nanotechnol.*, 2019, **19**, 826–832.
- 41 X. Tang, X. Hou, L. Yao, S. Hu, X. Liu and L. Xiang, *Mater. Res. Bull.*, 2014, **57**, 127–134.
- 42 M. Sukumar, L. John Kennedy, J. Judith Vijaya, B. Al-Najar and M. Bououdina, *Ceram. Int.*, 2018, **44**, 18113–18122.
- 43 D. V. Dharmadhikari, S. K. Nikam and A. A. Athawale, *J. Alloys Compd.*, 2014, **590**, 486–493.
- 44 M. Enhessari, M. Shaterian, M. J. Esfahani and M. N. Motaharian, *Mater. Sci. Semicond. Process.*, 2013, **16**, 1517–1520.
- 45 M. Sukumar, L. J. Kennedy, J. J. Vijaya, B. Al-najar and M. Bououdina, *J. Magn. Magn. Mater.*, 2018, **465**, 48–57.
- 46 Y. Gao, H. Chang, Q. Wu, Y. Liu, F. Liu, F. Zhu, Y. Pang and Y. Yun, *Curr. Appl. Phys. J.*, 2016, **16**, 922–926.
- 47 M. J. R. Hoch, S. Nellutla, J. Van Tol, E. S. Choi, J. Lu, H. Zheng and J. F. Mitchell, *Phys. Rev. B: Condens. Matter Mater. Phys.*, 2009, **79**, 214421.
- 48 S. Upadhyay, K. Parekh and B. Pandey, *J. Alloys Compd.*, 2016, **678**, 478–485.
- 49 R. D. Shannon, *Acta Crystallogr., Sect. A: Cryst. Phys., Diffr., Theor. Gen. Crystallogr.*, 1976, **32**, 751–767.
- 50 K. A. Cychosz, R. Guillet-Nicolas, J. García-Martínez and M. Thommes, *Chem. Soc. Rev.*, 2017, **46**, 389–414.
- 51 D. G. Lee, M. Kim, B. J. Kim, D. H. Kim, S. M. Lee, M. Choi, S. Lee and H. S. Jung, *Appl. Surf. Sci.*, 2011, **196**, 4370–4381.
- 52 S. Thanasilp, J. W. Schwank, V. Meeyoo, S. Pengpanich and M. Hunsom, *Chem. Eng. J.*, 2015, **275**, 113–124.
- 53 Z. I. Ishak, N. A. Sairi, Y. Alias, M. K. T. Aroua and R. Yusoff, *Chem. Eng. J.*, 2016, **297**, 128–138.
- 54 M. H. Haider, N. F. Dummer, D. W. Knight, R. L. Jenkins, M. Howard, J. Moulijn, S. H. Taylor and G. J. Hutchings, *Nat. Chem.*, 2015, **7**, 1028–1032.
- 55 S. Vajiček, M. Štolcová, A. Kaszonyi, M. Mičušík, P. Alexy, P. Canton, G. Onyestyák, S. Harnos, F. Lónyi and J. Valyon, *J. Ind. Eng. Chem.*, 2016, **39**, 77–86.
- 56 K. H. Lee and R. Hoffmann, *J. Phys. Chem. A*, 2006, **110**, 609–617.

- 57 S. Pesant and M. Côté, *Phys. Rev. B: Condens. Matter Mater. Phys.*, 2011, **84**, 085104.
- 58 A. M. Ritzmann, M. Pavone, A. B. Munoz-Garcia, J. A. Keith and E. A. Carter, *J. Mater. Chem. A*, 2014, **2**, 8060–8074.
- 59 D. Meng, H. Guo, Z. Cui, C. Ma, J. Zhao, J. Lu, H. Xu, Z. Wang, X. Hu, Z. Fu, R. Peng, J. Guo, X. Zhai, G. J. Brown, R. Knize and Y. Lu, *Proc. Natl. Acad. Sci. U. S. A.*, 2018, **115**, 2873–2877.
- 60 L. Qiao, J. H. Jang, D. J. Singh, Z. Gai, H. Xiao, A. Mehta, R. K. Vasudevan, A. Tselev, Z. Feng, H. Zhou, S. Li, W. Prellier, X. Zu, Z. Liu, A. Borisevich, A. P. Baddorf and M. D. Biegalski, *Nano Lett.*, 2015, **15**, 4677–4684.